Water Reflection Recognition Based on Motion Blur Invariant Moments in Curvelet Space

Sheng-Hua Zhong, Yan Liu, Yang Liu, and Chang-Sheng Li

***Abstract*— Water reflection, a typical imperfect reflection symmetry problem, plays an important role in image content analysis. Existing techniques of symmetry recognition, however, cannot recognize water reflection images correctly because of the complex and various distortions caused by the water wave. Hence, we propose a novel water reflection recognition technique to solve the problem. First, we construct a novel feature space composed of motion blur invariant moments in low-frequency curvelet space and of curvelet coefficients in high-frequency curvelet space. Second, we propose an efficient algorithm including two sub-algorithms: low-frequency reflection cost minimization and high-frequency curvelet coefficients discrimination to classify water reflection images and to determine the reflection axis. Through experimenting on authentic images in a series of tasks, the proposed techniques prove effective and reliable in classifying water reflection images and detecting the reflection axis, as well as in retrieving images with water reflection.**

***Index Terms*— Water reflection, imperfect symmetry, motion blur, invariant moments, reflection axis detection.**

I. Introduction

REFLECTION happens between two different medias. The direction of a wavefront at the interface changes so that the wavefront returns into the medium from which it is originated. In natural image analysis, water reflection plays an important role.

First, water reflection itself is an exciting natural landscape that attracts artists and photographers, so images with water reflection should be considered as one important category of natural images. Experiments from psychology reveal that subjects give favorable ratings to scenes with reflective water [1]. Many artists and photographers prefer works of water reflection image, e.g., "The Houses of Parliament, Sunset" which was painted by Claude Monet.

Second, the awareness of the existence of water reflection will greatly influence further analysis of an image, such as image segmentation and object recognition. Fig. 1(a) is an image with water reflection and the correct segmentation result is shown in Fig. 1(b). However, most existing segmentation algorithms, such as the state-of-the-art algorithms: graph-based technique, will consider the mountain and its reflection as one segment as shown in Fig. 1(c), if the existence of water reflection is not known prior to the analysis. As a result, the object mountain is not properly recognized due to the wrong segmentation. Obviously, the shape information in Fig. 1(c) will be helpless in detecting the mountain. Fig. 1(d) is the color histogram of the mountain part in Fig. 1(a), which is quite different from that of the combination of the mountain and the reflection as shown in Fig. 1(e). It is obviously that consider the object and the reflection as a whole will distort the color feature for recognition.

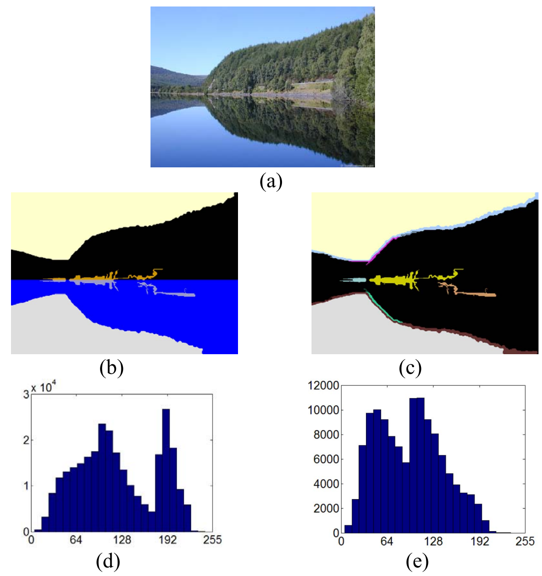

Fig. 1. Example of the influence from water reflection to image segmentation and object recognition by color histogram. (a) An example image with water reflection. (b) Desired segmentation result of the image. (c) Actual segmentation using existing algorithms. (d) Color histogram of the mountain. (e) Color histogram of the mountain and the reflection.

Third, water reflection is a special case of imperfect reflection symmetry. Symmetry is an essential and ubiquitous concept in nature, science, and art [2]. Issues relating to symmetry detection and recognition have attracted extensive attention in numerous fields including visual perception, computer vision, robotics, and computational geometry. In philosophy, symmetry is considered as a pre-attentive feature. This pre-attentive feature is useful to enhance recognition and reconstruction

Manuscript received September 12, 2012; revised February 26, 2013 and June 17, 2013; accepted June 21, 2013. Date of publication July 4, 2013; date of current version September 12, 2013. This work was supported in part by VideoGene-Robust and Scalable Fingerprint for Video Search and Mining Applications under Grant B-Q18S and HK PolyU under Grant 5245/09E. The associate editor coordinating the review of this manuscript and approving it for publication was Prof. Rafael Molina.

S.-H. Zhong, Y. Liu, and Y. Liu are with the Department of Computing, The Hong Kong Polytechnic University, 999077 Hong Kong (e-mail: csshzhong@comp.polyu.edu.hk; csyliu@comp.polyu.edu.hk; csygliu@comp.polyu.edu.hk).

C.-S. Li is with the Institute of Automation, Chinese Academy of Sciences, Beijing 100864, China (e-mail: csli@nlpr.ia.ac.cn).

Color versions of one or more of the figures in this paper are available online at http://ieeexplore.ieee.org.

Digital Object Identifier 10.1109/TIP.2013.2271851

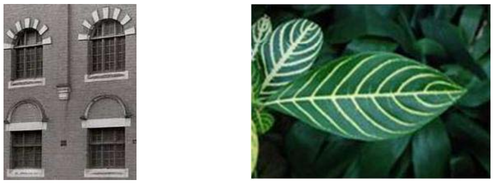

(a) (b)

Fig. 2. Examples of imperfect symmetry images. (a) is skewed symmetry. (b) is curved glide-reflection symmetry.

(a) (b)

Fig. 3. Examples of images containing water reflections of (a) incomplete and (b) indistinct shapes.

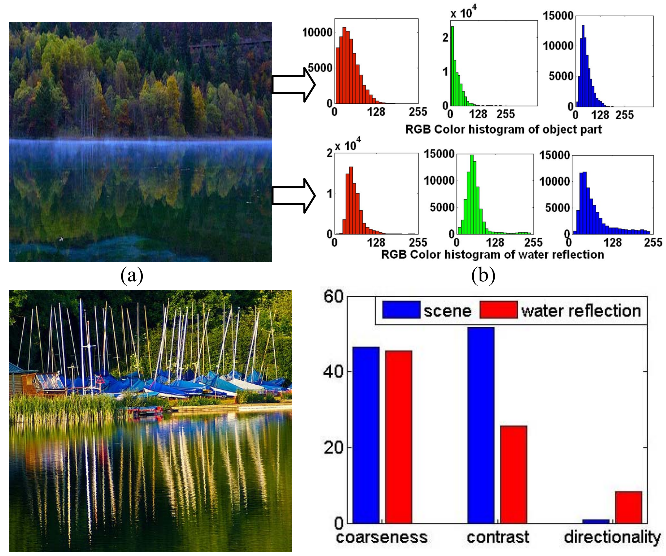

(a) (b) (c) (d)

Fig. 4. Feature distortion in water reflection images. (a) and (c) show the examples of water reflection images. (b) is the color histogram of object part and water reflection part in (a). (d) shows the texture features in the scene part and water reflection part of (a).

of shapes and objects [3]. Reflection symmetry is one of the common basic symmetries [4], in which one half of the object is indistinguishable from its mirror transformed image of the other. Reflection symmetry has been studied in many different fields for various applications from face analysis [5], vehicle detection [6] to medical image analysis [7]. Since the restriction to exact symmetries limits the use of these methods for real-world objects, more efforts have been focused on the imperfect symmetry [8], [9]. In water reflection images, the complexity of water part makes it impossible to keep the consistency between the object part and reflection part perfectly. Compared with other imperfect symmetry, such as skewed symmetry and curved glide-reflection symmetry in Fig. 2, water reflection has seldom been studied although it greatly influences the performance of natural image analysis. Moreover, some peculiar symmetry characters of water reflection make it worthy further exploring.

Although water reflection has great influence in many image processing tasks, currently, little research studies the water reflection images in view of vision [10]. To our knowledge, no effort has been made to address the classification, recognition and detection of water reflection images. Only one study has been carried out on detecting the water reflection axis in water reflection image [11]. The flip invariant shape detector utilized in [11] relies on the complete and distinct shape of water reflection part, which cannot be easily satisfied as water reflection is a complex phenomenon. For example, in Fig. 3(a) and (b), the snow mountain and trees are partially reflected because the ice above the water covers some area of the lake. Therefore, the method proposed in [11] cannot be successfully applied to many images containing nature water reflection. A short version of our preliminary work was published in [12] based on motion blur invariant moments. The preliminary work demonstrates good performance on water reflection recognition and reflection axis detection. But it has the limitation of distinguishing water reflection images from other imperfect symmetry images.

This paper formulates the water reflection recognition as a special case of imperfect reflection symmetry problem. To address the special characteristics of water wave, we construct a novel feature space that is composed of motion blur invariant moments in low-frequency Curvelet space and of Curvelet coefficients in high-frequency Curvelet space. With the help of moment invariants in low-frequency band, we could distinguish the imperfect symmetry images from other images. Utilizing Curvelet coefficients, water reflection images could be distinguished from other imperfect symmetry images. Based on the novel feature space, we propose an efficient algorithm including two sub-algorithms: Low-frequency Reflection Cost Minimization (LRCM) and High-frequency Curvelet Coefficients Discrimination (HCCD). This algorithm is effective and reliable to classify water reflection images from other images and to determine the reflection axis. Moreover, this algorithm has lower computational complexity than exhaust algorithm.

The rest of the paper is organized as follows. Section II discusses the limitations of existing feature space used in symmetry detection and recognition tasks. Then, we propose a new feature space based on the characteristics of water waves. Section III provides an efficient solution to solve the problem of classification and recognition of water reflection images. Section IV reports the experiments on authentic datasets. Finally, the paper draws on conclusion in Section V.

II. Feature Space in Water Reflection Recognition

The key to address the difficulty in water reflection recognition is to find out the effective and robust feature descriptors. First, let us observe the distortion due to the water reflection in the most commonly used feature space. Fig. 4(a) and Fig. 4(b) demonstrate the color distortion of the forest after reflection. Obviously, much of the red information is lost. In Fig. 4(d),

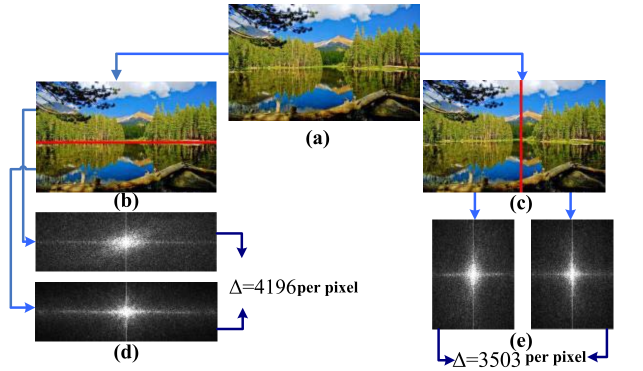

Fig. 5. An example of features from Fourier domain based on the image (a). (b) and (d) show the Fourier transform with real reflection axis. (c) and (e) show the Fourier transform with fake reflection axis.

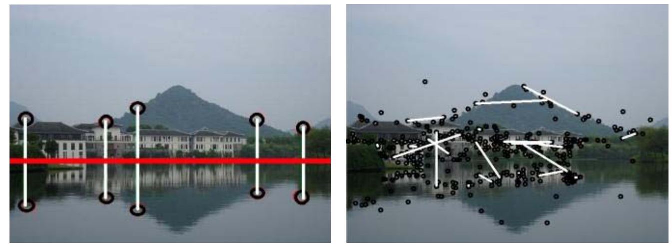

Fig. 6. An example of SIFT saliency points detection and matching. (a) is the desired result (b) is the real result of SIFT descriptor detection and matching.

three most important Tamura texture features from the scene part and water reflection part of Fig. 4(c) are compared, which are most popular features selected by psychological experiments [13]. There exist great differences of contrast and directionality between the original one and its reflection.

Therefore, in water reflection images, the distortion in feature space is widespread To address the difficulty of water reflection recognition, we first review the limitations of using the existing features in symmetry detection and recognition for water reflection tasks. Then we analyze the distortion caused by motion blur of the water part in feature space. Third, we propose a novel feature space called Invariant Moment & Curvelet Coefficient feature space (IMCC).

A. Limitation of Existing Feature Space for Water Reflection Recognition

Based on the nature of the features extracted from images, the existing algorithms for reflection symmetry detection and recognition can be roughly classified into two general approaches [14], namely, the global approaches and the local approaches.

In global approaches, features from Fourier domain are the most commonly used for global approach of reflection symmetry detection and recognition. For example, Lucchese [15] proposed an elegant approach to analyze the angular properties of an image in Fourier domain. Derrode et al. [16] analyzed the symmetries of real objects by computing the Analytic Fourier-Mellin transform (AFMT). Their methods are based on the idea that Fourier transform preserves the symmetry of images in the Fourier domain. Let $I(\mathbf{x}), \mathbf{x} = [x\, y]^{\mathrm{T}} \in \mathbb{R}^2$ denote the scalar image of 2-D pattern. In [15], Lucchese proved that if an image having reflection symmetry with respect to the reflection axis $y = x \times \tan\alpha$, its Fourier transform $I(\omega), \omega \in \mathbb{R}^2$ has the same reflection symmetry with respect to the line $\omega_y = \omega_x \times \tan\alpha$. The difference between the original one and the reflection one will be much smaller than the difference between other parts. But due to the characteristics of the water part, this conclusion is not always true. Fig. 5(a) shows an example image with water reflection. Fig. 5(b) is the image with the correct reflection axis. We calculate the Fourier transform with this reflection axis. Based on Fig. 5(d) which is the Fourier transform $I(\omega)$ results of object part and water reflection part, we find the $I(\omega)$ does not have the reflection symmetry as expected. The average difference of object part and water reflection part is much larger than fake symmetry axis marked in Fig. 5(c).

Because the use of local features is among the corner stones of modern computer vision, recent work starts emphasizing the use of local image features. The representative one is scale-invariant feature transform (SIFT) descriptor. Loy *et al.* [17] chose SIFT detection points as interesting salient points and took advantage of pairwise matching of their SIFT descriptors to detect the axis of symmetry. Some other existing work focused on the shape characteristics of symmetry [18]. For example, local invariants were computed as single points on the curves [19], [20] or statistically compare pairs of contour points [21], [22].

For local approaches of reflection symmetry detection and recognition, SIFT descriptor is the most representative feature. As shown in Fig. 6(a), the desired result is that the SIFT saliency points are matched in pairs between the object and its reflection. Fig. 6(b) shows the real SIFT points detection and matching result using algorithm in [17]. Obviously, it is difficult to recognize the water reflection by matching the SIFT points.

B. Feature Distortion Caused by Motion Blur

As we described in earlier sections, existing feature space utilized in symmetry detection and recognition is invalid to the task of water reflection recognition. Motion blur is considered to be one of the important causes.

Motion blur is the apparent streaking of rapidly moving objects in a still image or a sequence of images such as a movie or animation. The formation model for the motion blur is:

$$g(\mathbf{x}) = I(\mathbf{x}) * h(\mathbf{x}) + n(\mathbf{x}) \tag{1}$$

where $\mathbf{x} = (x, y) \in \mathbb{R}^2$ denotes the coordinates of an image pixel, I denotes the original image, $h(\mathbf{x})$ is the point spread function (psf), $n(\mathbf{x})$ is additive noise, g represents the observed image, and the symbol $*$ stands for the 2D convolution operation. Assume that translation motion function $\mathbf{M}(t) = [M_x(t), M_y(t)]$ is known, $h(\mathbf{x})$ has the following form (2):

$$h(\mathbf{x}) = \frac{1}{t_e}\int_{t_o}^{t_o+t_e} \delta(\mathbf{x} - \mathbf{M}(t))dt \tag{2}$$

(a) (b)

Fig. 7. An example of the motion blur effect in water reflection image with different exposure time (b) has a longer exposure time to (a).

where the Dirac delta function describes the two-dimensional displacement function of the image during the exposure interval (t_0, t_0+t_e), where t_e denotes the exposure period, and $1/t_e$ is a normalizing factor.

Motion blur happens when the image being recorded changes during the recording of a single image, either due to rapid movement or long exposure [23]. To the case of water reflection, motion blur is a result of the interplay between the speed of oscillation of the surface waves and the camera's limited shutter speed. If image shows a perfect instant in time (analogous to a camera with an infinitely fast shutter), zero motion blur will be generated. But with the technological constraints, this is not the real case. Usually, when a sensor creates an image, that image does not represent a single instant of time. And a fast moving object or a longer exposure time may result in blurring artifacts which make this apparent just as Fig. 7. These two images are downloaded from Digitalcameraworld [24]. According to the description in the webpage, the only difference of them is the exposure time. Both of the images have some degree of motion blur, and the motion blur in Fig. 7(b) is very obvious.

Shutter speed or exposure time is the effective length of time a sensor's shutter is open [25]. The human eye can form 10–12 images per second [26]. The agreed standards of cameras for shutter speeds are from 1/1000 second to 1 second [27]. According to the relationship of object distance u and focal length f, the motion in image could be denoted as $\Delta d = \Delta x \times (f/u)$, where Δx is the motion of the object. Δx can be calculated as the product of the exposure time t_e and the velocity υ of specific point in the wave profile. As an example of 1/4 CCD, if the size of image is 640×480 pixels (30M), the pixel size is equal to 5×5 μm. We assume the object distance u is 100 meters and velocity υ of specific point in the wave profile is equal to 0.3 m/sec. Taking the shutter speeds range into consideration, in this case, the maximum motion in image is about 30 pixels. If the object distance is 20 meters, the maximum motion in image is about 150 pixels. If conventional cameras' exposure time 1/30 second is selected as the exposure time and the object distance is 20 meters, the motion is about 5 pixels. It is large enough to change the image features needed for feature-based recognition.

Although the research on water reflection is very limited, some image processing applications shed light on the existence of motion blur. There is a general consensus in image processing applications' community that adding motion blur is a necessary step in faking water reflection images. How to add motion blur to construct realistic water reflection image is described in the introduction shown in Photoshopdaily, 10steps.sg and other well known websites for the Photoshop community [28], [29].

Motion blur changes the image features needed for feature-based recognition techniques [30]. Furthermore, motion blur causes a decay of the information and energy in high-frequency band. The change of high-frequency information in water reflection is one reason for the invalidity of existing global algorithms in Fourier domain [15]. In summary, the theoretical analysis, image processing applications and experiment of different exposure time all support the motion blur exists in water reflection in general, while the effect is relied on the exposure time. We believe there are other factors can distort the feature space and will influence the classification performance further, such as light dispersion on the wavy surface. Here, we only consider the motion blur degradation.

To analyze the influence of the motion blur in water reflection, we need to have a fundamental understanding of water wave. Water wave could be considered as being composed of a great quantity of periodic progressive waves. Simply speaking, a periodic progressive wave is characterized by the amplitude A, wavelength λ, phase velocity V_p, mean fluid depth H, and period $T (T = \lambda/V_p)$. Actually, real water wave is exceedingly complex as it is also influenced by the depth of water, the velocity of wind, and so on.

The complex water wave problem could be effectively simplified into a boundary value problem by Newman [31]. According to the differential equation with the conditions at the boundaries (bottom boundary conditions and free surface boundary conditions), the small amplitude wave functions could be denoted as Eq. 3 in two dimensional x-z plane. In Eq. 3, ϑ is the velocity potential, g_r is the gravitational acceleration, and η is the wave profile which means the position of the water surface.

$$\begin{cases} \frac{\partial^2\vartheta}{\partial x^2} + \frac{\partial^2\vartheta}{\partial z^2} = 0 & -H < z < \eta, \quad -\infty < x < +\infty \\ \frac{\partial\vartheta}{\partial z} = 0 & z = -H \\ \eta = -\frac{1}{g_r}\left.\frac{\partial\vartheta}{\partial t}\right|_{z=0} & \end{cases} \tag{3}$$

After solving the wave functions utilizing the method of variables separation, we could get the function of wave profile in Eq. 4 and phase velocity in Eq. 5. And the velocity of every point in the wave profile could be denoted as Eq. 6.

$$\eta = A\cos(2\pi x/\lambda - 2\pi t/T) \tag{4}$$

$$V_p = \sqrt{\frac{g_r L}{2\pi}\tanh\frac{2\pi H}{\lambda}} \tag{5}$$

$$\begin{cases} \upsilon_x = 2\pi A\frac{\cosh 2\pi(z+H)/\lambda}{T\sinh 2\pi H/\lambda}\cos(2\pi x/\lambda - 2\pi t/T) \\ \upsilon_z = 2\pi A\frac{\sinh 2\pi(z+H)/\lambda}{T\sinh 2\pi H/\lambda}\sin(2\pi x/\lambda - 2\pi t/T) \end{cases} \tag{6}$$

Based on Eq. 4, we could conclude that the surface of water part has different offsets in position due to the water wave. The offset in position leads to the ineffectiveness of exiting symmetry algorithms based on local features.

As we known, motion blur could be removed from images with the help of deconvolution, which is often adopted in the literature for motion blur detection and recognition. But the core idea in deconvolution is to calculate the point spread function, assuming that the velocity and direction of motion blur is unique [32], [33]. Eq. 5 and Eq. 6 indicate obviously that the motion in the water is ubiquitous, and that the velocity of different position with different frequency is various too Therefore, the necessary assumption of deconvolution methods is invalid. Thus, none of existing techniques is effective to this situation, which necessitates effective feature space to address the issues resulted from motion blur.

C. Invariant Moment and Curvelet Coefficient Feature Space

As we described before, the key to water reflection recognition is effective feature space that is utilized to address the problem resulted from motion blur. Based on the characteristics of water reflection, the task of water reflection recognition could be separated into two parts, the first of which is to distinguish imperfect symmetry images and the second is to distinguish water reflection images from imperfect symmetry images. Therefore, the proposed feature space has two components focus on these two requirements respectively.

The first component of proposed feature space is the motion blur invariant moments in low-frequency Curvelet space. This feature channel is utilized to distinguish imperfect symmetry images with other images.

Moment invariants were first introduced to the pattern recognition and image processing community in 1962 [34], when Hu employed the results of the theory of algebraic invariants and derived his seven famous invariants to the rotation of 2D objects. Since then, moment invariants have become one of the most important and most frequently used descriptors. There have been numerous papers on moment invariants to affine and projective transforms, to photometric changes and to linear filtering of an image.

Image moments are weighted averages (moments) of the image pixels' intensities, or functions of those moments, usually chosen to have some attractive property or interpretation [35]. Compared with color histogram, the shift of moment due to the change of illumination will be minimal [36], which also often happens in water part.

General moment M_{pq} of an image I is defined as:

$$M_{pq} = \iint\limits_{D} p_{pq}(x, y) I(x, y) dx dy \tag{7}$$

where p, q are non-negative integers $r = p + q$ is called the order of the moment, and $p_{pq}(x, y)$ is the polynomial basis function. The most common choice is a standard power basis $p_{pq}(x, y) = x^p y^q$ that leads to geometric moments:

$$m_{pq} = \int_{-\infty}^{\infty} \int_{-\infty}^{\infty} x^p y^q I(x, y) dx dy \tag{8}$$

The central moments are defined as:

$$\mu_{pq} = \int_{-\infty}^{\infty} \int_{-\infty}^{\infty} (x - \overline{x})^p (y - \overline{y})^q I(x, y) dx dy \tag{9}$$

where $\overline{x} = m_{10}/m_{00}$ and $\overline{y} = m_{01}/m_{00}$ are the components of the centroid. If I is a digital image, Eq. 8 and Eq. 9 are changed to Eq. 10 and Eq. 11.

$$m_{pq} = \sum_{x} \sum_{y} x^p y^q I(x, y) \tag{10}$$

$$\mu_{pq} = \sum_{x} \sum_{y} (x - \overline{x})^p (y - \overline{y})^q I(x, y) \tag{11}$$

Moments η_{pq} where $p + q \geq 2$ can be constructed to be invariant to both translation and changes in scale by dividing the corresponding central moment by the properly scaled (00)th moment, using the following formula:

$$\eta_{pq} = \frac{\mu_{pq}}{\mu_{00}^{\left(1+\frac{p+q}{2}\right)}} \tag{12}$$

Based on [37], the following four moment invariants could be proved invariant to linear motion convolution. Therefore, these moment invariants are also invariant to motion blur.

$$\begin{cases} IR_{m_1} = (\eta_{30} - 3\eta_{12})^2 + (3\eta_{21} - \eta_{03})^2 \\ IR_{m_2} = (\eta_{30} + \eta_{12})^2 + (\eta_{21} + \eta_{03})^2 \\ IR_{m_3} = (\eta_{30} - 3\eta_{12})(\eta_{30} + \eta_{12})[(\eta_{30} + \eta_{12})^2 - 3(\eta_{21} + \eta_{03})^2] \\ \quad + (3\eta_{21} - \eta_{03})(\eta_{21} + \eta_{03})[3(\eta_{30} + \eta_{12})^2 - (\eta_{21} + \eta_{03})^2] \\ IR_{m_4} = (3\eta_{21} - \eta_{03})(\eta_{30} + \eta_{12})[(\eta_{30} + \eta_{12})^2 - 3(\eta_{21} + \eta_{03})^2] \\ \quad + (\eta_{30} - 3\eta_{12})(\eta_{21} + \eta_{03})[3(\eta_{30} + \eta_{12})^2 - (\eta_{21} + \eta_{03})^2] \end{cases} \tag{13}$$

The most important property of invariant features is invariance. Based on the analysis before, the moment invariants are satisfied with this property. In moment invariants feature space, the difference between the object part and the distorted part due to motion blur is not large. Another desirable property of invariant features is discriminability. Unfortunately, moment invariants are not useful to distinguish water reflection from imperfect symmetry.

Therefore, the second problem is how to distinguish water reflection images from other imperfect symmetry images. As we described before, motion blur causes a decay of the information and energy in high-frequency band. If our feature space effectively measures the existence of this phenomenon, we could distinguish water reflection images from imperfect images successfully. For this end, we utilize the Curvelet coefficients in high-frequency as one component of proposed feature descriptors. The Curvelet transform is a multiscale pyramid with many directions and positions at each length scale, and needle-shaped elements at fine scales. As the latest multi-directional & multi-scale transform, Curvelet was developed in an attempt to overcome inherent limitations of traditional multiscale representations such as wavelets [38]. Compared with wavelet transform, Curvelet transform has subtle capability to represent directional features in image [39].

For water reflection images, the object part contains a wealth of details in various directions, but the reflection part has a decay of the information and energy in high-frequency band. To describe the difference fully and accurately, our technique is based on the Curvelet coefficients in high-frequency band. In Curvelet transform, the work is throughout in two dimensions, i.e., $\mathbb{R}^2$, with spatial variable $\mathbf{x} = (x, y) \in \mathbb{R}^2$, with the frequency domain variable ω, and with r and θ polar coordinates

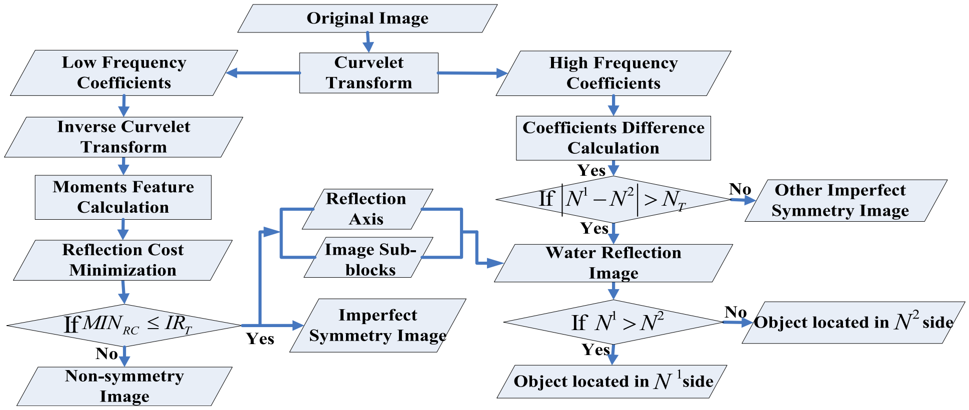

Fig. 8. The flowchart of proposed algorithm LRCM-HCCD.

in the frequency-domain. The basic pair of windows includes the "radial window" $W(r)$ with $r \in (1/2, 2)$ and "angular window" $V(t)$ with $t \in [-1, 1]$. Then, the frequency window U_a is defined in the Fourier domain as follows:

$$U_a(r, \theta) = 2^{-3a/4} W(2^{-a} r) V\left(\frac{2^{\lfloor a/2 \rfloor}\theta}{2\pi}\right) \tag{14}$$

where $a = 0, 1, \ldots$ is a scale parameter, $\lfloor a/2 \rfloor$ is the largest integer below $a/2$. The support of U_a is a polar "wedge" defined by W and V which is applied with scale-dependent window widths in each direction.

Define the waveform $\varphi_a(\mathbf{x})$ by means of its Fourier transform $\hat{\varphi}_a(\omega) = U_a(\omega)$ $\omega = (\omega_x, \omega_y) \in \mathbb{R}^2$ is utilized by letting $U_a(\omega_x, \omega_y)$ be the window defined in the polar coordinate system. The equispaced sequence of rotation angle is denoted as $\theta_\upsilon = 2\pi \cdot 2^{-\lfloor a/2 \rfloor} \cdot \upsilon$, with the orientation parameter $\upsilon = 0, 1, \ldots$ such that $0 \leq \theta_\upsilon \leq 2\pi$. And the sequence of translation parameter is denoted as $b = (b_x, b_y) \in \mathbb{Z}^2$. With these notations, the Curvelets are defined as function of $\mathbf{x} = (x, y) \in \mathbb{R}^2$ at scale 2^{-a}, orientation θ_υ and position $\mathbf{x}_{a,\upsilon,b} = R_{\theta_\upsilon}^{-1}(b_x \cdot 2^{-a}, b_y \cdot 2^{-a/2})$ by Eq. 15,

$$\varphi_{a,\upsilon,b}(\mathbf{x}) = \varphi_a(\mathbf{R}_{\theta_\upsilon}(\mathbf{x} - \mathbf{x}_{a,\upsilon,b})) \tag{15}$$

where $\mathbf{R}_\theta$ is the rotation by θ radians as follows

$$\mathbf{R}_\theta = \begin{pmatrix} \cos\theta & \sin\theta \\ -\sin\theta & \cos\theta \end{pmatrix} \tag{16}$$

So the Curvelet coefficient map $c_{a,\upsilon,b}(x, y)$ is then simply the inner product between an element $I(x, y) \in L^2(\mathbb{R}^2)$ of image and a Curvelet $\varphi_{a,\upsilon,b}$.

$$c_{a,\upsilon,b}(x, y) = \langle I(x, y), \varphi_{a,\upsilon,b} \rangle \tag{17}$$

In digital Curvelet Transforms, similar with the continuous-Time Curvelet transform, U_a smoothly extracts frequencies near the dyadic corona $\{2^a \leq r \leq 2^{a+1}\}$ and near the angle $\{-\pi \cdot 2^{-a/2} \leq \theta \leq \pi \cdot 2^{-a/2}\}$. But due to the fact that the coronae and rotation are not especially adapted to Cartesian arrays, in digital Curvelet transform, the "Cartesian coronae" based on the concentric squares and shears are utilized. With scale parameter $a = 10$, the high-frequency spectral band is composed of 64 cartesian coronas, and every corona is corresponding to a specific direction υ, $\upsilon = 1, 2 \ldots 64$. The Curvelet coefficient map $c_{a,\upsilon,b}$ to every coronae could be calculated by Eq. 17. The absolute values of the coefficients indicate the strength of the information in specific direction.

In our proposed feature space, the Curvelet coefficients in high-frequency band to every coronae is denoted as $\mathbf{CC}_\upsilon$, $1 \leq \upsilon \leq 64$.

III. Algorithm

In Section II, we have discussed the limitations of existing feature space and proposed Invariant Moment & Curvelet Coefficient (IMCC) feature space according to the characteristics of motion blur. Based on the feature space, in this section, we propose two effective sub-algorithms to recognize the water reflection image, including: Low-frequency Reflection Cost Minimization (LRCM) and High-frequency Curvelet Coefficients Discrimination (HCCD).

Fig. 8 presents the flowchart of the proposed algorithm LRCM-HCCD. It includes two channels, the low-frequency and high-frequency Curvelet channels. To the first channel, the Curvelet transform is utilized to obtain the low frequency coefficients. We then calculate the moment invariants after using the inverse Curvelet transform on the low frequency coefficients. Based on the moment invariants, we minimize the reflection cost using dynamic programming (DP) and distinguish the imperfect images from non-symmetry images. To the second channel, the high-frequency Curvelet coefficients are obtained by Curvelet transform. According to the differences of the coefficients in the image sub-blocks located in both sides of reflection axis water reflection and imperfect symmetry images are classified into two categories. Furthermore, the object part and the reflection part are then distinguishable from each other.

A. Imperfect Symmetry Recognition by Low-Frequency Reflection Cost Minimization

In this part, we introduce the sub-algorithm Low-frequency Reflection Cost Minimization (LRCM) for imperfect symmetry recognition. The definition of reflection symmetry is given first.

Definition 1: A set $S \in \mathrm{R}^n$ is reflection symmetric with respect to the vector (reflection axis) $< \cos\alpha_0, \sin\alpha_0 >$ with a reflection transform T_{D_K}, if $\forall \mathbf{x}_i \in S, \exists \mathbf{x}_j \in S$, $s.t$,

$$\mathbf{x}_j = T_{D_K}\mathbf{x}_i \tag{18}$$

where for $\mathbf{x}_i \in \mathbb{R}^2$, T_{D_K} is given by

$$T_{D_K}(x, y) = \begin{pmatrix} \cos 2\alpha_0 & \sin 2\alpha_0 & 0 \\ \sin 2\alpha_0 & -\cos 2\alpha_0 & 0 \\ 0 & 0 & 1 \end{pmatrix} \begin{pmatrix} x \\ y \\ 1 \end{pmatrix} \tag{19}$$

So a centered image I, if it has the reflection symmetry with the reflection axis $< \cos\alpha_0, \sin\alpha_0 >$, obeys the Eq. 20.

$$I(\mathbf{x}) = I(T_{D_K}(\mathbf{x})) \qquad \forall \mathbf{x} \in \mathbb{R}^2 \tag{20}$$

In most conditions concerning imperfect reflection symmetry, Eq. 20 could not be strictly complied with imperfect symmetry, meaning that in water reflection case, $I(\mathbf{x}) \approx I(T_{D_K}(\mathbf{x})), \forall \mathbf{x} \in \mathbb{R}^2$.

Based on the analysis in Section II, we transform the imperfect symmetry problem into an optimization problem based on the complex moment invariants feature space given by Eq. 21.

$$\begin{cases} \alpha_0^* = \arg\min |\sum_{i=1}^{4} IR_{m_i}(I(\mathbf{x})) - \sum_{i=1}^{4} IR_{m_i}(I(T_{D_K}(\mathbf{x})))| \\ \min \left| \sum_{i=1}^{4} IR_{m_i}(I(\mathbf{x})) - \sum_{i=1}^{4} IR_{m_i}(I(T_{D_K}(\mathbf{x}))) \right| \leq IR_{thresh} \end{cases} \tag{21}$$

where IR_{thresh} is the threshold to distinguish imperfect symmetry images from non-symmetry images, and α_0^* is the tilt angle of the reflection axis.

The motion blur invariants are effective based on the linear motion which is valid in local range. But in nature, the velocity of water in different location with different frequency is various. In our paper, we solve this dilemma by restricting the moment features calculation into sub-blocks. We divide the image into sub-blocks, and we assume the velocity of the water in every reflection image block keep constant, or the difference is small. Furthermore, water reflection or other imperfect symmetry often does not occur in the whole image and the reflection axis is usually not complete or straight. Taking these situations into consideration, we do some simplifications based on the optimized problem shown in Eq. 21.

Images are separated into M_s sub-images vertical to the supposed reflection axis direction DI_{α_0}. For every sub-image $I_j, 1 \leq j \leq M_s$, the candidate reflection axis is denoted as $RA_{j,l}, 1 \leq j \leq M_s, 1 \leq l \leq H_{\alpha_0}$, where H_{α_0} is the height of the sub-image I_j. The sum difference of the moment invariants $DF_{j,k,l}$ of the image block $I^1_{j,k,l}(\mathbf{x})$ and its reversed block $I^2_{j,k,l}(\mathbf{x})$ located on both sides of line $RA_{j,l}$ is given in Eq. 22:

$$DF_{j,k,l} = \sum_{i=1}^{4}\sum_{p}^{P}[IR_{m_i}(sub^{1,p}_{j,k,l}(\mathbf{x})) - IR_{m_i}(sub^{2,p}_{j,k,l}(\mathbf{x}))] \tag{22}$$

where $sub^{1,p}_{j,k,l}(\mathbf{x})$ is the p-th sub-block of $I^1_{j,k,l}(\mathbf{x})$, $sub^{2,p}_{j,k,l}(\mathbf{x})$ is the reversed sub-block of $sub^{1,p}_{j,k,l}(\mathbf{x})$ in $I^2_{j,k,l}(\mathbf{x})$. P is the number of sub-block in image block $I^1_{j,k,l}(\mathbf{x})$. k is the height of sub-block which is above the threshold T_k.

Reflection axis distance $DS_{j,l}$ is utilized to measure the continuity of the adjacent reflection axis denoted as Eq. 23.

$$DS_{j,l} = \begin{cases} \left\| RA_{j.l} - RA_{j+1.l} \right\| / T_d + 1 & j \leq M_s - 1 \\ 1 & j = M_s \end{cases} \tag{23}$$

In this equation, $\|RA_{j.l} - RA_{j+1.l}\|$ is used to describe the vertical distance between the candidate reflection axis in adjacent sub-image I_j and I_{j+1}. T_d is the factor used to normalize the distance to an specified range.

We define the reflection cost RC in the current slide window SW_m, $1 \leq m \leq H_{\alpha_0} - W_{sw}$ which is decided by $DF_{j,k,l}$ and $DS_{j,l}$ in Eq. 24. The slide window SW_m with width W_{sw} is horizontal to the candidate reflection axis direction. The location of the centerline in SW_m is denoted as L_m and $L_m = m + W_{sw}/2$. The minimum of the reflection cost RC in all slide windows is denoted as MIN_{RC}. The optimized reflection axis, which is composed of RA_{j,l^*} in every sub-image I_j of slide window SW^*_m with the minimum of the reflection cost, is denoted as Eq. 25.

$$RC = \sum_{j=1}^{M_s}(DF_{j,k,l} \times DS_{j,l}), \quad T_k \leq k \leq \frac{H_{\alpha_0}}{2}, \quad l \in SW_m, \\ 1 \leq m \leq H_{\alpha_0} - W_{sw}, \quad -\frac{\pi}{2} \leq \alpha_0 \leq \frac{\pi}{2} \tag{24}$$

$$[\alpha_0^*, SW^*_m, RA_{1,l^*}, RA_{2,l^*}, \ldots RA_{M_s,l^*}] = \arg\min\left[\sum_{j=1}^{M_s}(DF_{j,k,l} \times DS_{j,l})\right] \tag{25}$$

The aim of this optimization problem is to find MIN_{RC} and the optimal reflection axis with the corresponding sub-blocks.

The optimization problem we described in Eq. 24 and Eq. 25 is similar as the one that is often solved by dynamic programming (DP). DP is both a mathematical optimization method and a computer programming method. In both contexts DP refers to simplifying a complicated problem by breaking it down into simpler sub-problems in a recursive manner. We have a preprocessing work before DP to limit the number of candidate reflection axis $RA_{j,l}$ in every sub image I_j. Then we rank the differences of moment invariants $DF_{j,k,l}$ and only those $RA_{j,l}$ whose difference falls into the M_n minimum value are considered as the candidate reflection axis.

Then we define some basic concepts and variables in DP for water reflection problem. The *Stage variable* $K = j$, $1 \leq j \leq M_s$ is used to describe the current stage or sub-image. The *State variable* λ_K in our algorithm $\lambda_K = RA_{j,l}$ is the candidate reflection axis in the sub-image I_j. The *decision variable* u_K in our case, is the choice of the candidate reflection axis $RA_{j+1,l}$ in the next sub image I_{j+1}. The *Transition function* is defined as $\lambda_{K+1} = \mu_K$. The *Object function* is defined as Eq. 26 where υ_K is the minimum of reflection cost in stage K denoted in Eq. 27.

$$V = \sum_{K=1}^{M_s}\upsilon_K(\lambda_K, \mu_K) \tag{26}$$

$$\upsilon_K = \min[DF_{j,k,l} \times DS_{j,l}]$$

Algorithm 1 Classification Accuracy Results

Input: Image I, Number of sub-block M_s, Height threshold T_k, Number of candidate axis M_n, Normalization factor T_d, Height of sub-image H_{α_0}, Width of slide window W_{sw}.

Output: Minimum moment cost MIN_{RC}

1. Sum difference of moment invariants calculation

 for $\alpha_0 = -\pi/2, ..., \pi/2$ **do**

  for $j = 1, ..., M_s$ **do**

   for $l = 1, ..., H_{\alpha_0}$ **do**

    for $k = T_k, ..., H_{\alpha_0}/2$ **do**

$$DF_{j,k,l} = \sum_{i=1}^{4} \sum_{p}^{P} [IR_{m_i}(sub_{j,k,l}^{1,p}(\mathbf{x})) - IR_{m_i}(sub_{j,k,l}^{2,p}(\mathbf{x}))]$$

    end for

   end for

  end for

 end for

2. Sort $DF_{j,k,l}$ for every α_0 in ascending manner, choose whose value fallen into the first M_n minimum as candidate axis $RA_{j,l}$
3. Reflection axis distance $DS_{j,l}$ calculation

$$DS_{j,l} = \begin{cases} \left\| RA_{j,l} - RA_{j+1,l} \right\| / T_d + 1 & j \le M_s - 1 \\ 1 & j = M_s \end{cases}$$

4. Minimum moment cost in stage K calculation

$$v_K = \min[DF_{j,k,l} \times DS_{j,l}]$$

$$s.t.\ K = j, T_k \le k \le \frac{H_{\alpha_0}}{2}, l \in SW_m, 1 \le m \le H_{\alpha_0} - W_{sw}, -\frac{\pi}{2} \le \alpha_0 \le \frac{\pi}{2}$$

5. Minimum moment cost calculation for every α_0

$$\begin{cases} f_K(\lambda_K) = \min\{v_K(\lambda_K, \mu_K) + f_{K-1}(\lambda_{K-1})\} \\ \lambda_K \in \Lambda_K \qquad K = j, 1 \le j \le M_s \\ \lambda_{K+1} = \mu_K \end{cases}$$

6. Minimum moment cost MIN_{RC} calculation

$$MIN_{RC} = \min(f_{M_S}(\lambda_{M_s})), 1 \le m \le H_{\alpha_0} - W_{sw}, -\frac{\pi}{2} \le \alpha_0 \le \frac{\pi}{2}$$

$$s.t.\ K = j, T_k \le k \le \frac{H_{\alpha_0}}{2}, l \in SW_m, 1 \le m \le H_{\alpha_0} - W_{sw}, -\frac{\pi}{2} \le \alpha_0 \le \frac{\pi}{2} \tag{27}$$

The DP function is defined using Eq. 28,

$$\begin{cases} f_K(\lambda_K) = \min\{v_K(\lambda_K, \mu_K) + f_{K-1}(\lambda_{K-1})\} \\ \lambda_K \in \Lambda_K \qquad K = j, 1 \le j \le M_s \\ \lambda_{K+1} = \mu_K \end{cases} \tag{28}$$

where $f_K(\lambda_K)$ is the minimum of the reflection cost in every stage K in current SW_m. Then we solve the Eq. 28 by positive sequence method to get the optimized policy in current slide window SW_m. After that, MIN_{RC} that is the minimum of all RC in different slide windows and in different α_0 is calculated by Eq. 29.

$$MIN_{RC} = \min(f_{M_S}(\lambda_{M_s})), 1 \le m \le H_{\alpha_0} - W_{sw}, -\frac{\pi}{2} \le \alpha_0 \le \frac{\pi}{2} \tag{29}$$

The algorithm of LRCM is described in Algorithm 1.

We also compare the difference of computational complexity between exhaust algorithm and our DP algorithm. For simplicity, we only calculate that the computational complexity to find the optimization axis in direction α_0. If the exhaust algorithm is utilize to find the global optimization axis in Eq. 25, the complexity is: $O((W_{sw}^{M_s} + W_{sw}^{M_s} \times \log_2(W_{sw}^{M_s})) \times H_{\alpha_0})$. To the proposed algorithm, the complexity is: $O((M_s - 1) \times W_{sw}^2 \times \log_2(W_{sw}^2) \times H_{\alpha_0})$. It is obvious that the total computational complexity of DP is much lower than that of exhaust algorithm.

B. Water Reflection Recognition by High-Frequency Curvelet Coefficients Discrimination

Water reflection is a special case of imperfect symmetry. The algorithm proposed to distinguish imperfect symmetry with non-symmetry is provided in Part A of Section III. To further the proposal, the optimized reflection axis with the corresponding sub-blocks is obtained. In this part, we propose the sub-algorithm High-frequency Curvelet Coefficients Discrimination (HCCD) to distinguish water reflection images from imperfect symmetry images.

As we described in Part B of Section II, one important characteristic of motion blur is that it causes a decay of the information and energy in high-frequency band. Therefore, we focus on the high-frequency Curvelet coefficients to address distinguishability of water reflection images from other imperfect symmetry images.

After the Curvelet transform, the Curvelet coefficients in high-frequency band $\mathbf{CC}_v$, $1 \le v \le 64$ is calculated to every coronae. As we known, the absolute values of the coefficients indicate the strength of the information in specific direction Therefore, for every direction, the differences of the absolute value between every optimized sub-blocks located in both sides of optimized reflection axis are calculated by Eq. 30.

$$\mathbf{DC}_{K,v} = \left|\mathbf{CC}_{K,v}^1\right| - \left|\mathbf{CC}_{K,v}^2\right| \tag{30}$$

where $\mathbf{CC}_{K,v}^1$ and $\mathbf{CC}_{K,v}^2$ are denoted as the Curvelet coefficients in high-frequency band for direction v and sub-block pair I_K^1 and I_K^2 in stage K.

To every sub-block pair, we calculate the sum of the absolute value $sp_{K,v}$ and $sn_{K,v}$ in positive and negative part of $\mathbf{DC}_{K,v}$, respectively.

$$\begin{cases} sp_{K,v} = \text{abs}[\sum_{m,n} DC_{K,v}(m,n)] \text{ if } DC_{K,v}(m,n) > 0 \\ sn_{K,v} = \text{abs}[\sum_{m,n} DC_{K,v}(m,n)] \text{ if } DC_{K,v}(m,n) < 0 \end{cases} \tag{31}$$

We count the number of positive Curvelet coefficients in object part and in its reflection part, just as Eq. 32

$$\begin{cases} np_K = \sum_{v=1}^{64} \left[\varepsilon(\left|sp_{K,v}\right| - \left|sn_{K,v}\right|)\right] \\ nn_K = \sum_{v=1}^{64} \left[\varepsilon(\left|sn_{K,v}\right| - \left|sp_{K,v}\right|)\right] \end{cases} \tag{32}$$

where $\varepsilon(n)$ is the unit step function, and $\varepsilon(n) = \begin{cases} 1 \text{ if } n \ge 0 \\ 0 \text{ if } n < 0 \end{cases}$. If to arbitrary k, the absolute difference between np_K and nn_K is larger than T_n, the image is water reflection. Otherwise, it is imperfect symmetry.

Furthermore, in water reflection images, the comparison of np_K and nn_K is helpful to distinguish between the object part

Fig. 9. Sample images with water reflection in classification experiment.

Fig. 10. Sample images without water reflection in classification experiment.

and the reflection part. Compared with the reflection part, the object part has more high-frequency information. Therefore, we could tell the object part from its reflection part easily. If to arbitrary k, np_K is greater than nn_K, I^1 is the object part; otherwise, I^2 is the object part.

IV. Experiments

To demonstrate the performance of our proposed technique, we conduct three experiments, including the classification of nature scene images with and without water reflection, the detection of reflection axis, and the retrieval of water reflection images. In our experiments, for the size of image sub-block, it is difficult to determine the most suitable value. In our implement, we utilized 64 × 64 as the size of image block based on two reasons. First, with this size, the calculation of the moment features can be retained in a local region. Second, it will limit the computational cost of the moment features [40]. I also utilized other values as the size of image block, such as 56 × 56, 48 × 48. It shows stable performance under these values. To the parameters, we set $T_k = 64$, $T_d = H_{\alpha_0}/12$, $M_n = H_{\alpha_0}/4$, $T_n = 35$, $W_{sw} = H_{\alpha_0}/25$, and M_s is the largest integer number of the sub-block in the supposed reflection axis direction DI_{α_0}.

A. Water Reflection Image Classification

In the first experiment, to evaluate the classification accuracy of the proposed technique, we construct a dataset including 50 images with water reflection and 50 nature scene images without water reflection. Fig. 9 and Fig. 10 present the thumbnails of images with and without water reflection respectively, all of which are utilized in the first experiment.

We subdivide this dataset equally into five folders, and conduct fivefold cross validations for the learning algorithms. Every time, we utilize one folder for testing, and the other four folders for training. If MIN_{RC} is below the threshold IR_{thresh} which is learnt by binary SVM classifier based on the training dataset, this image is classified as the water reflection image. The classification accuracy results are provided in Table I. The results prove that our proposed technique based on IMCC features could effectively distinguish the water reflection images from other nature scene images. To evaluate the effectiveness of the proposed moment features, we also provide the classification accuracy using the same algorithm LRCM-HCCD but based on color histogram. Here, WR stands for water reflection images and NWR stands for non water reflection images.

TABLE I

Classification Accuracy Results

Trail	1	2	3	4	5
WR based on moments	90%	90%	90%	100%	90%
NWR based on moments	80%	70%	80%	90%	80%
Overall based on moments	85%	80%	85%	95%	85%
WR based on color histogram	60%	70%	60%	70%	60%
NWR based on color histogram	50%	50%	70%	80%	70%
Overall based on color histogram	55%	60%	65%	75%	65%

TABLE II

Detection Accuracy Results

Distance(pixels)	5	20	50	100
SIFT based technique	18%	29%	33%	41%
Shape based technique	36%	46%	70%	88%
LRCM-HCCD	73%	87%	99%	100%

B. Detection the Reflection Axis

To compare with existing symmetry techniques, the detection experiment is carried out on 100 images with water reflection where groundtruth reflection axes are provided by human subjects. The goal of this experiment is to detect the reflection axis. We first compare our technique with the representative technique of Loy et al. [17], which utilized the SIFT detection points as interesting salient points and took advantage of pairwise matching of their SIFT descriptors to detect the axis of symmetry. We also compare ours with the only paper on detection of water reflection axis proposed by Zhang *et al.* based on the shape detector [11] To evaluate different techniques, we use the average Euclidean distance from all the points on the detected axis to the corresponding points on the ground truth reflection axis. The detection accuracy results are provided in Table II. The proposed technique LRCM-HCCD performs robustly with different distance threshold.

Examples results are given in Fig. 11 to illustrate the reflection axis detection results of the three techniques. To our proposed technique, not only the axis detection results are provided, the object and reflection regions' boundaries are also given by green curve. Although these boundaries do not cover all of the objects and reflection, the effective and clear object and corresponding reflection are involved. The regions' boundaries with the reflection axis provide the hint to further image analysis, such as segmentation.

Due to the limitations of SIFT detectors and descriptors discussed in Section II, it is predictable that the accuracy of the technique [17] is low. The technique [11] utilized

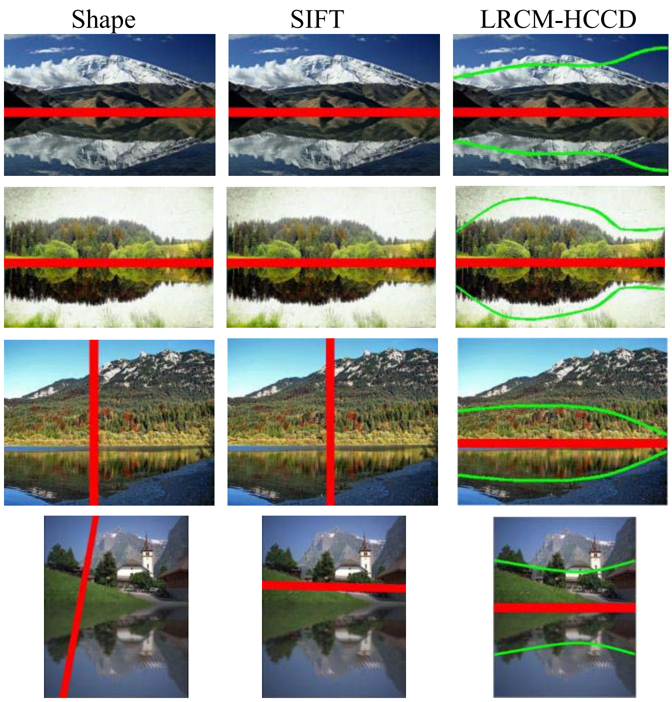

Fig. 11. Performance comparison of reflection axis detection. First, second and third column are the results of Shape, SIFT and LRCM-HCCD respectively.

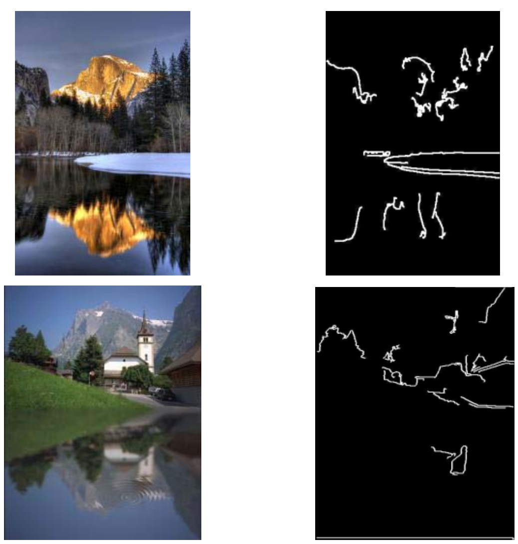

Fig. 12. Examples of shape detection result of invariant shape technique.

the flip invariant shape detector relying on the completeness of the shape. Unfortunately, water reflection is a complex and various phenomena often with incomplete and distorted shape in reflection part, which leads to the ineffectiveness of technique [11] just as two examples in Fig. 12.

C. Water Reflection Image Retrieval Experiment

We then apply the proposed technique in text based image retrieval for evaluation. The textual query is "water reflection", every image that is related to this concept is returned. The dataset is downloaded from Google and is composed of two parts. The first part is 50 images with water reflection, and the second part contains 10000 images without water reflection. Fig. 13 shows the thumbnails of images with and without water reflection used in the retrieval experiment. Different from the nature scene images utilized in classification experiment, the images in the retrieval experiment are more diversified, and include imperfect symmetry images.

Fig. 13. Sample images with & without water reflection in retrieval experiment.

TABLE III
PRECISION AND RECALL RESULTS

Retrieval Number	10	20	30	40	50
Precision without Curvelet	70%	70%	73%	73%	72%
Recall without Curvelet	14%	28%	44%	58%	72%
Precision with Curvelet	90%	90%	90%	83%	86%
Recall with Curvelet	18%	36%	54%	66%	86%

Many different measures for evaluating the performance of image retrieval systems have been proposed. In our experiment, we use four popular ones: precision, recall, AveP and NDCG. Precision is defined as the fraction of the images retrieved that are relevant to the user's information need in the information retrieval system. Recall is the fraction of the images that are relevant to the query that are successfully retrieved.

$$\text{Precision} = (N_{Relevant} \cap N_{Retrieved})/N_{Retrieved} \quad (33)$$

$$\text{Recall} = (N_{Relevant} \cap N_{Retrieved})/N_{Relevant} \quad (34)$$

where $N_{Relevant}$ is the number of images which are relevant to the query and $N_{Retrieved}$ is the number of images that are finally retrieved out.

In the proposed technique, the Curvelet coefficients in high-frequency part are utilized to distinguish the water reflection image from the imperfect symmetry image. In this dataset, we first demonstrate the retrieval performance with or without the contribution of Curvelet coefficients part. Table III shows the Precision and Recall comparison results. The number of retrieval sample is from 10 to 50 with increments of 10. It is obviously that the highfrequency coefficients are helpful to achieve a better classification. Two examples of imperfect symmetry images which are correctly distinguished by Curvelet coefficients are given in Fig. 14.

Precision and recall are single-value metrics based on the whole list of multimedia documents returned by the retrieval system. For systems that return a ranked sequence of images, it is also desirable to consider the order in which the returned images are presented. Average precision emphasizes ranking relevant images higher and is computed in Eq. 35 at the point

Fig. 14. Examples of imperfect symmetry images that are correctly distinguished by Curvelet coefficients.

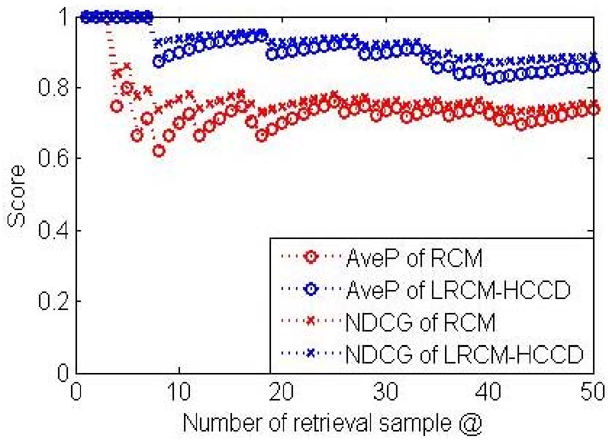

Fig. 15. AveP and NDCG results of the retrieval experiment.

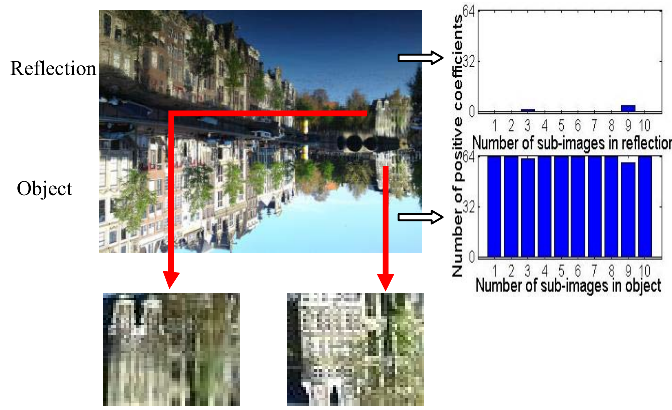

(a)

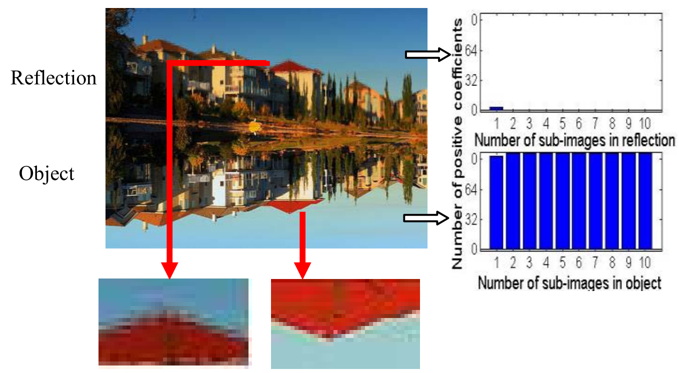

(b)

Fig. 16. Object and reflection parts determined by the Curvelet coefficients. (a) Reversed water reflection image with positive Curvelet coefficients of reflection and object part. (b) Reversed water reflection image with positive Curvelet coefficients of reflection and object parts.

of each of the relevant images in the ranked sequence,

$$\text{AveP@}p = \frac{\sum_{i=1}^{p}(P_i \times Rel_i)}{N_{Relevant}} \tag{35}$$

where p is the rank position Rel_i is a binary function on the relevance of a given rank, and P_i is the precision at a given cut-off rank where $N_{RR}(i)$ is the number of relevant retrieved images of rank i or less:

$$P_i = \frac{N_{RR}(i)}{i} \tag{36}$$

The premise of DCG is that relevant documents appearing lower in a search result list should be penalized, as the graded relevance value is reduced logarithmically with a proportion to the position of the result. The DCG accumulated at a particular rank position p is defined as Eq. 37. For a query, the normalized discounted cumulative gain, or NDCG, is computed as Eq. 38, where IDCG is the ideal DCG at position p. Fig. 15 shows the AveP and NDCG scores of LRCM-HCCD and RCM [12]. Compared with the existing proposed technique only based on minimizing the reflection cost, the proposed technique has better discriminative ability.

$$\text{DCG@}p = Rel_1 + \sum_{i=2}^{p}\frac{Rel_i}{\log_2 i} \tag{37}$$

$$\text{NDCG@}p = \frac{\text{DCG@}p}{\text{IDCG@}p} \tag{38}$$

D. Discussion

According to the three experiments and a series of evaluations, our proposed feature descriptors and techniques are proven effective in water reflection detection and recognition. Moreover, our technique has an additional advantage in detecting which part is the object in water reflection images Fig. 16 gives two sample images from our dataset, both of which have been uploaded upside down. Due to the similarity of object and reflection parts, such case is even difficult to be detected by human eyes in the original image size. As described in Section II, the object part tends to have larger Curvelet coefficients in high-frequency band. Thus a comparison of Curvelet coefficients located on the both sides of the reflection axis could help determine the object part easily and correctly.

V. Conclusion

Water reflection is a special case of imperfect reflection symmetry problem, but no existing techniques have been proposed to address the task of water reflection image classification. To address this problem, we propose a novel feature space Invariant Moment & Curvelet Coefficient (IMCC) according to the characteristics of motion blur in water reflection images. An effective and efficient water reflection classification and reflection axis detection technique is then constructed based on

IMCC. Experiments and evaluation all confirmed the effectiveness and robustness of our technique, which is more reliable and successful compared with existing feature space and algorithms. In future, we are interested in investigating how to model, estimate or remove other possible degradation in water reflection, such as light dispersion on the wavy surface. We want to analyze the influence of different degradations and explore a novel technique to distinguish different distortions from motion blur or from light dispersion.

REFERENCES

[1] J. L. Nasar and M. H. Li, "Landscape mirror: The attractiveness of reflecting water," *Landscape Urban Planning*, vol. 66, no. 4, pp. 233–238, Feb. 2004.

[2] M. Chertok and Y. Keller, "Spectral symmetry analysis," *IEEE Trans. Pattern Anal. Mach. Intell.*, vol. 32, no. 7, pp. 1227–1238, Jul. 2010.

[3] F. Attneave, "Symmetry information and memory for patterns," *Amer. J. Psychol.*, vol. 68, no. 2, pp. 209–222, Jun. 1955.

[4] H. Wey, *Symmetry*. Princeton, NJ, USA: Princeton Univ. Press, 1952.

[5] S. Mitra and Y. X. Liu, "Local facial asymmetry for expression classification," in *Proc. IEEE Conf. Comput. Vis. Pattern Recognit.*, Jun. 2004, pp. 889–894.

[6] A. Kuehnle, "Symmetry-based recognition of vehicle rears," *Pattern Recognit. Lett.*, vol. 12, no. 4, pp. 249–258, Apr. 1991.

[7] M. Mancas, B. Gosselin, and B. Macq, "Fast and automatic tumoral area localisation using symmetry," in *Proc. IEEE ICASSP Conf.*, vol. 2. Mar. 2005, pp. 725–728.

[8] Q. Guo, F. L. Guo, and J. Q. Shao, "Irregular shape symmetry analysis: Theory and application to quantitative galaxy classification," *IEEE Trans. Pattern Anal. Mach. Intell.*, vol. 32, no. 10, pp. 1730–1743, Oct. 2010.

[9] J. Podolak, A. Golovinskiy, and S. Rusinkiewicz, "Symmetry-enhanced remeshing of surfaces," in *Proc. Symp. Geometry Process.*, Jul. 2007, pp. 1–8.

[10] P. P. Huang, C. F. Chen, and J. H. Wang, "Experimental studies of several reflection detection methods," *Energy Procedia*, vol. 13, no. 2011, pp. 6776–6781, 2011.

[11] H. Zhang, X. J. Guo, and X. C. Cao, "Water reflection detection using a flip invariant shape detector," in *Proc. Int. Conf. Pattern Recognit.*, Aug. 2010, pp. 633–636.

[12] S. H. Zhong, Y. Liu, L. Shao, and F. L. Chung, "Water reflection recognition via minimizing reflection cost based on motion blur invariant moments," in *Proc. 1st ACM Int. Conf. Multimedia Retr.*, 2011.

[13] H. Tamura, S. Mori, and T. Yamawaki, "Texture features corresponding to visual perception," *IEEE Trans. Syst., Man, Cybern.*, vol. 8, no. 6, pp. 460–473, Jun. 1978.

[14] A. D. Gross and T. E. Boult, "Analyzing skewed symmetries," *Int. J. Comput. Vis.*, vol. 13, no. 1, pp. 91–111, Sep. 1994.

[15] L. Lucchese, "Frequency domain classification of cyclic and dihedral symmetries of finite 2-D patterns," *Pattern Recognit.*, vol. 37, no. 12, pp. 2263–2280, Dec. 2004.

[16] S. Derrode and F. Ghorbel, "Shape analysis and symmetry detection in gray-level objects using the analytical Fourier–Mellin representation," *Signal Process.*, vol. 84, no. 1, pp. 25–39, Jan. 2004.

[17] G. Loy and J. Eklundh, "Detecting symmetry and symmetric constellations of features," in *Proc. Eur. Conf. Comput. Vis.*, May 2006, pp. 508–521.

[18] V. S. N. Prasad and B. Yegnanarayana, "Finding axes of symmetry from potential fields," *IEEE Trans. Image Process.*, vol. 13, no. 12, pp. 1559–1556, Dec. 2004.

[19] L. Vangool, T. Moons, D. Ungureanu, and E. Pauwels, "Symmetry from shape and shape from symmetry," *Int. J. Robot. Res.*, vol. 14, no. 5, pp. 407–424, Oct. 1995.

[20] L. Vangool, T. Moons, D. Ungureanu, and A. Oosterlinck, "The characterization and detection of skewed symmetry," *Comput. Vis. Image Understand.*, vol. 61, no. 1, pp. 138–150, Jan. 1995.

[21] T. J. Cham and R. Cipolla, "Symmetry detection through local skewed symmetries," *Image Vis. Comput.*, vol. 13, no. 5, pp. 439–450, Jan. 1995.

[22] K. S. Y. Yuen and W. W. Chan, "Two methods for detecting symmetries," *Pattern Recognit. Lett.*, vol. 15, no. 3, pp. 279–286, Mar. 1994.

[23] J. Flusser, T. Suk, and S. Saic, "Recognition of images degraded by linear motion blur without restoration," in *Computing Supplementum*, vol. 11. New York, NY, USA: Springer-Verlag, 1996, pp. 37–51.

[24] J. Meyer. (2012). *Making the Case for Auto ISO* [Online]. Available: http://www.digitalcameraworld.com/2012/07/18/making-the-case-for-auto-iso/

[25] F. R. Sidney, "Camera features," in *Manual of Photography: A Textbook of Photographic and Digital Imaging*. Waltham, MA, USA: Focal Press, 2000, pp. 131–132.

[26] P. Read and M. P. Meyer, "Restoration of Motion picture film," in *Conservation and Museology*. Oxford, U.K.: Butterworth-Heinemann, 2000, pp. 24–26.

[27] C. Kahn, *Essential Skills for Nature Photography*. Amherst, MA, USA: Amherst Media, 1999.

[28] J. Cole. (2009). *Fake a Water Reflection* [Online]. Available: http://www.photoshopdaily.co.uk/featured/fake-a-water-reflection/

[29] A. Chua. (2012). *A Realistic Water Reflections Photoshop Tutorial* [Online]. Available: http://10steps.sg/tutorials/photoshop/a-realistic-water-reflections-photoshop-tutorial/

[30] A. Stern, I. Kruchakov, E. Yoavi, and N. S. Kopeika, "Recognition of motion-blurred images by use of the method of moments," *Appl. Opt.*, vol. 41, no. 11, pp. 2164–2171, 2002.

[31] J. N. Newman, *Marine Hydrodynamics*. Cambridge, MA, USA: MIT Press, 1977.

[32] X. Y. Qi, L. Zhang, and C. L. Tan, "Motion deblurring for optical character recognition," in *Proc. Int. Conf. Document Anal. Recognit.*, Sep. 2005, pp. 389–393.

[33] J. Hui and C. Q. Liu, "Motion blur identification from image gradients," in *Proc. Int. Conf. Comput. Vis. Pattern Recognit.*, Jun. 2008, pp. 1–8.

[34] M.-K. Hu, "Visual pattern recognition by moment invariants," *IRE Trans. Inf. Theory*, vol. 8, no. 2, pp. 179–187, Feb. 1962.

[35] K. H. Abas and O. Ono, "Implementation of multi-centroid moment invariants in thermal-based face identification system," *Amer. J. Appl. Sci.*, vol. 7, no. 3, pp. 283–289, 2010.

[36] M. K. Mandal, T. Aboulnasr, and S. Panchanathan, "Image indexing using moments and wavelets," *IEEE Trans. Consum. Electron.*, vol. 42, no. 3, pp. 557–565, Aug. 1996.

[37] J. Flusser, T. Suk, and B. Zitová, *Moments and Moment Invariants in Pattern Recognition*, New York, NY, USA: Wiley, 2009.

[38] E. J. Cand'es and D. L. Donoho, "New tight frames of curvelets and optimal representations of objects with piecewise C^2 singularities," *Commun. Pure Appl. Math.*, vol. 52, no. 2, pp. 219–266, Feb. 2004.

[39] K. Feng, Z. N. Jiang, W. He, and B. Ma, "A recognition and novelty detection approach based on Curvelet transform, nonlinear PCA and SVM with application to indicator diagram diagnosis," *Expert Syst. Appl.*, vol. 38, no. 10, pp. 12721–12729, Sep. 2011.

[40] R. Ferzli and L. J. Karam, "A no-reference objective image sharpness metric based on the notion of just noticeable blur (JNB)," *IEEE Trans. Image Process.*, vol. 18, no. 4, pp. 717–728, Apr. 2009.

Sheng-Hua Zhong received the B.Sc. degree in optical information science and technology from the Nanjing University of Posts and Telecommunication, Nanjing, China, in 2005, and the M.S. degree in signal and information processing from Shenzhen University, Guangdong, China, in 2007. She is currently pursuing the Ph.D. degree from the Department of Computing, The Hong Kong Polytechnic University, Hong Kong. Her current research interests include multimedia content analysis and cognitive science.

Yan Liu received the B.Eng. degree from the Department of Electrical Engineering, Southeast University, Nanjing, China, the M.Sc. degree from the School of Business, Nanjing University, Nanjing, and the Ph.D. degree from the Department of Computer Science, Columbia University, New York, NY, USA. She is an Associate Professor with the Department of Computing, The Hong Kong Polytechnic University, Hong Kong. Her current research interests include multimedia content analysis, machine learning, and cognitive science.

Yang Liu received the B.Sc. and M.Sc. degree in automation from the National University of Defense Technology, Changsha, China, in 2004 and 2007, respectively, and the Ph.D. degree from the Department of Computing, The Hong Kong Polytechnic University, Hong Kong, in 2011. His current research interests include machine learning, pattern recognition, digital video processing and analysis, and multimedia content retrieval and summarization.

Chang-Sheng Li received the B.S. degree in electronic engineering from the University of Electronic Science and Technology of China, Chengdu, China, in 2008. He is currently pursuing the Ph.D. degree in computer science with the Institute of Automation, Chinese Academy of Sciences, Beijing, China. His current research interests include machine learning, pattern recognition, and multimedia content analysis.